

State-of-the-art of chemically grown vanadium pentoxide nanostructures with enhanced electrochemical properties

Dimitra Vernardou*

Center of Materials Technology and Photonics, School of Applied Technology, Technological Educational Institute of Crete, 710 04 Heraklion, Crete, Greece

*Corresponding author. Tel: (+30) 2810 379774; E-mail: dimitra@iesl.forth.gr

Received: 22 May 2013, Revised: 29 June 2013 and Accepted: 01 July 2013

ABSTRACT

This review begins by the principles that describe the intercalation properties of vanadium pentoxide. Recent developments in the chemical synthesis of vanadium pentoxide nanostructures including nanorod and nanotube arrays, nanowires, anhydrous and hydrous nanorolls and nanobelts, nanoribbons, nanocables and gels are examined. The objective of this review is to demonstrate the use of these nanostructures as cathodes for lithium batteries and electrochromics with high storage capacity and rate performance due to the large surface area and short distance for charge transport compared to the thin film cathodes. Copyright © 2013 VBRI press.

Keywords: Vanadium pentoxide; nanostructures; intercalation properties; batteries; electrochromics.



Dimitra Vernardou is a member of “Center of Materials Technology and Photonics” laboratory in Technological Educational Institute of Crete. She obtained her B.Sc. in Chemistry from University of Salford in 2000, her M.Sc. in Polymer Science and Technology from UMIST (Manchester) in 2001 and her Ph.D. in Physical Chemistry from University of Salford in 2005. She has experience in the chemical growth and structural, as well as optical and morphological characterization of pure and/or doped metal oxide thin films. Her current research interests involve oxide growth as nanostructures with tuneable characteristics in terms of size and shape and band gap energy, using low cost easily scalable techniques such as hydrothermal growth, electrodeposition and atmospheric pressure chemical vapour deposition, for thermochromic, electrochromic, self-cleaning and capacitor applications.

1. Introduction

Vanadium pentoxide is a typical intercalation compound because of the multiple valence state of vanadium and the rich structural chemistry, which enables redox-dependent properties [1]. The intercalation refers to the reversible insertion of guest species into a host lattice that contains an interconnected system of an empty lattice site of appropriate size, while the structural integrity of the host lattice is formally conserved. When guest species are incorporated into host lattices, various structural changes take place. The principle geometrical transitions of host lattice matrixes upon intercalation of guest species include: a) change in interlayer spacing, b) change in stacking mode of the layers and c) formation of intermediate phases at low guest concentrations that may exhibit staging [2].

The intercalation reactions take place with a large free energy of formation, which has led to their use as the cathodes in lithium batteries [3]. Concomitant with the species insertion, electrons are introduced into the conduction bands giving rise to changes in colour. This ready colouration under ambient conditions led to their use in electrochromic displays [4].

This review will be concerned with the recent developments in the synthesis of nanostructured vanadium pentoxide. The relationship between the structure and properties with the electrochemical behaviour as relevant to batteries and electrochromics will be discussed. The impact of morphology and size will be described as there is much interest in nano-sized structures for diffusion controlled

reactions where diffusion length and properties may be a function of size.

1.1. How do the lithium batteries operate?

A battery is a device that converts chemical potential to electric energy through Faradaic reactions, which includes heterogeneous charge transfer occurring at the surface of an electrode [5]. It consists of three basic components: an anode, a cathode and an electrolyte. It is broadly grouped as primary and secondary battery. A primary battery is a single-use device and cannot be recharged, while a secondary battery can be recharged for many times.

The principal concept of lithium batteries is shown in **Fig. 1**. An anode (source of the lithium ions) with a cathode (sink for the lithium ions) having a more positive redox potential gives a lithium transfer cell. They are separated by the electrolyte, which is a lithium ion conductor. It provides the separation of ionic and electronic transport. Upon charging, lithium ions are released by the cathode and intercalated at the anode. While upon discharging, lithium ions are extracted by the anode and inserted into the cathode. Cathode materials must fulfil the following requirements to reach the goal of a high energy density (expressed in Wh L⁻¹) [6]: (1) a high number of available charge carriers per mass and volume unit, (2) a high cell voltage, resulting from a high (cathode) and low (anode) standard redox potential of the respective cathode redox reaction, (3) a high reversibility of electrochemical reactions at both cathodes and anodes to maintain the specific charge for hundreds of charge-discharge cycles, (4) stability, i.e. no degradation upon cycling, (5) low cost and (5) environmentally benign.

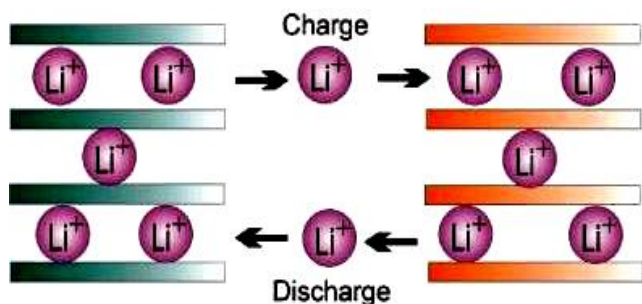


Fig. 1. A schematic presentation of a lithium battery, taken from [7].

Currently there are three intercalation materials that are used commercially as cathode materials in lithium batteries: LiCoO₂, LiNiO₂ and LiMn₂O₄. Among those, LiCoO₂ is the most popular because of the simplicity of its preparation [8]. The Li_xCoO₂ system has been studied extensively thus far exhibiting excellent cyclability at room temperature for 1 > x > 0.5. The specific capacity of the material is limited to the range 137–140 mAh g⁻¹, although the theoretical capacity of LiCoO₂ is 273 mAh g⁻¹ [9]. Even though it has good electrochemical properties and is easy to synthesize, it is very expensive and highly toxic. On the other hand, the reversible capacity of Li_xNiO₂ is higher than that of Li_xCoO₂, since the amount of lithium that can be intercalated / extracted during redox cycles is around 0.55 in comparison with 0.5 for LiCoO₂, allowing the specific capacity to be more than 150 mAh g⁻¹ with appropriate

cyclability [10]. Although LiNiO₂ and LiCoO₂ are isostructural, the preparation of LiNiO₂ is more complicated. Since there are additional nickel ions on the lithium sites and vice versa in the crystal structure of LiNiO₂, the Li–Ni–O system is represented by Li_{1-y}Ni_{1+y}O₂, a deviation from the normal stoichiometry [11]. In comparison with LiCoO₂ and LiNiO₂, LiMn₂O₄ is less toxic and has an abundant source. In principle, Li_xMn₂O₄ permits the intercalation / extraction of lithium ions in the range 0 < x < 2 [12]. For values of x between 1 and 2, the material consists of two different phases—cubic in the bulk and tetragonal at the surface. Simultaneously, the intercalation of lithium ions effectively decreases the average valence of manganese ions and leads to a pronounced cooperative Jahn–Teller effect, in which the cubic spinel crystal becomes distorted tetragonal with c/a ≈ 1.16, and the volume of the unit cell increases by 6.5 %. This high c/a ratio causes a low capacity restricted to <120–125 mAh g⁻¹ and significant capacity degradation at moderate temperatures in the range of 50–70 °C [13].

The limitations of the cathode materials have stimulated research activity targeted at investigating new materials for lithium batteries [14]. Vanadium pentoxide has attracted much interest because it offers the advantages of being cheap, easy to synthesize and having high energy densities. Electrochemical lithium ion intercalation occurs together with compensating electron intercalation, leading to the formation of vanadium bronzes as follows in equation (1):



However, the intercalation capacity and charge / discharge rate of V₂O₅ are limited by the low diffusion coefficient of Li ions (10⁻¹²–10⁻¹³ cm² s⁻¹) in the V₂O₅ matrix [15]. Many studies have been conducted to improve lithium diffusion and electrical conduction performance in V₂O₅ including nanostructured materials that possess large surface areas and short diffusion paths. Ordered arrays of nanorods, nanotubes or nanocables are some of the most promising nanostructures for lithium intercalation applications. Patrissi and Martin investigated the electrochemical properties of V₂O₅ nanorod arrays, which achieved four times the capacity of a thin-film cathode at high discharge rate [16]. Compared to nanorods, nanotubes possess higher surface area due to their several different areas of contact, i.e., the inner and outer wall surfaces, as well as the open ends. In addition, they can operate as electrolyte-filled channels for faster transport of the ions to the intercalation sites.

Another approach to increase the intercalation capacity of vanadium pentoxide is to modify its interlayer structure and the interaction forces between the adjacent layers. When the distance between the adjacent V₂O₅ layers increases, the insertion capacity increases. For example, V₂O₅·nH₂O possesses a lithium intercalation capacity that is about 1.4 times larger than that of V₂O₅ [17]. The distance between the adjacent layers in V₂O₅·nH₂O is 11.52 Å [18], compared to an interlayer distance of 4.56 Å in orthorhombic V₂O₅. Doping or substitution in V₂O₅ by other cations with different valence states have been used to tailor the interaction forces between two adjacent layers in the intercalation compound. Several materials, such as Ni

[19], Ce [20], Ag, and Cu [21], have been reported to enhance the capacity of V_2O_5 by forming bronze structures with it.

1.2. What are the electrochromics?

Electrochromics can be darkened (reflecting light) or lightened (transmitting light) in response to an electric field (Fig. 2). They are made by sandwiching certain materials between two panes of glass or plastic as listed below:

- Glass or plastic panel
- Conducting oxide
- Electrochromic layer
- Ion conductor / electrolyte
- Ion storage
- Conducting oxide
- Glass or plastic panel

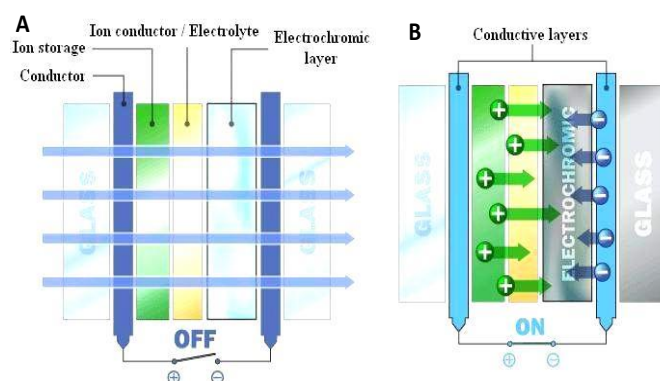


Fig. 2. (a) When the system is switched off, the electrochromic window is transparent. (b) When the system is switched on, the electrochromic window is dark, taken from [22].

The general electrochromic requirements are the following:

- A minimum contrast ratio 5:1 of the clear state (bleached) to the darkened (colored) state.
- Good cyclic lifetime (>100000 cycles).
- Continuous range in heat and optical transmittance, reflectance and absorbance between bleached and coloured states.
- Colouring and bleaching times of a few seconds.
- Switching with applied voltages 1-5 V.
- Large area with optical clarity.
- Sustained performance over 20-30 years.
- Acceptable cost (70 €/m²).

Numerous transition metal oxides possess the electrochromic property [4]: a decrease of transmittance occurs upon ion insertion in oxides of Ti, Nb, Mo, Ta and W, while an increase of the transmittance upon ion insertion in oxides of Cr, Mn, Fe, Co, Ni, Rh and Ir. Among those, tungsten trioxide appears to be the best electrochromic material. Its advantages are high colouration efficiency, reasonable stability and relatively low cost. Nevertheless, for building applications, the bright blue colour of WO_3 in the reduced state is not as favourable as

neutral gray or bronze colours. Hence, the need for materials exhibiting a different colour from that of WO_3 is important to extend the range of functions of electrochromics.

In this case, electrochromic vanadium pentoxide has attracted a lot of interest. This oxide is special in that charge insertion increases the transmittance in the ultraviolet and short-wavelength parts of the luminous spectrum, while it drops the transmittance in the long-wavelength part of this spectrum as well as in the near infrared [23-31].

However, the kinetics of ion insertion is limited by solid state lithium ion diffusion. Reducing the length of the diffusion path by designing a highly porous network is a desirable approach to address this issue. In the case of vanadium pentoxide, gels serve as host materials for a wide variety of metal cations [32]. The large lithium insertion capacity of vanadium pentoxide xerogels, theoretically up to two equivalent of lithium per vanadium, makes them attractive for use as cathodes in electrochromic devices. In addition, the capacity of lithium intercalation at high discharge rates can be improved by controlling the size and shape of the individual particles and the morphology of the V_2O_5 . For example, the rate capabilities of the nanostructured cathodes were compared with the rate capabilities of thin film cathodes showing that the nanostructured cathodes delivered higher capacities than the thin film cathodes [2]. This is because the nanostructured cathode has a short Li-ion insertion / extraction distance, facile strain relaxation upon electrochemical cycling, and very large surface to volume ratio to contact with the electrolyte, which can improve its capacity and cycle life. Hierarchical nanostructured materials such as hollow nanospheres, porous nanostructures, nanotubes, nanowire structures, and kinked nanowires, etc., can ensure that surface remains uncovered to keep the effective contact areas large even if a small amount of inevitable self-aggregation occurs. Moreover, if one dimension of the nanocrystallites is up to a few hundred micrometers or even at millimeter scale, such as ultralong nanowires or nanobelts, self-aggregation of the nanomaterials can be effectively prevented. Therefore, to some extent, an ultralong hierarchical nanowire is one of the most favourable structures as cathode materials.

2. Characteristics of vanadium pentoxide

2.1. Structure and properties of crystalline V_2O_5 upon lithium insertion

Orthorhombic crystalline V_2O_5 consists of layers of VO_5 square pyramids that share edges and corners [12] (see Fig. 3). The vanadium-oxygen bond distance is much shorter than the four other distances and corresponds to a double bond illustrating a two-dimensional character of this material. In addition, the structure of V_2O_5 can be described as distorted VO_6 octahedral, which emphasizes the structural relationship to ReO_3 via crystallographic shears [33]. The very large length of the sixth vanadium-oxygen bond underlines the structural anisotropy of this material and the ability to insert guest species perovskite-like cavities.

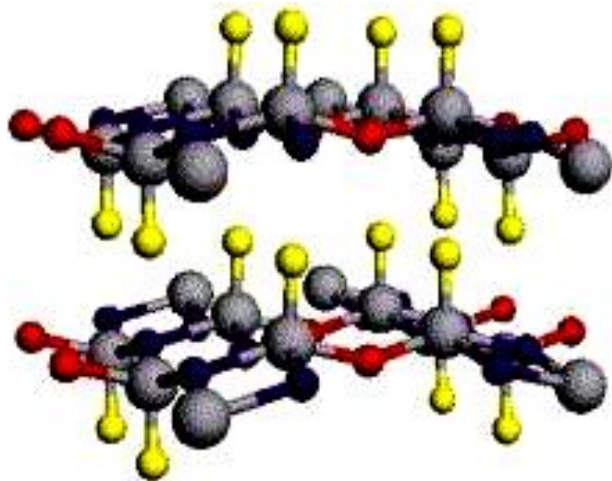


Fig. 3. Schematic presentation of V_2O_5 layered structure. The grey circle presents vanadium centres, yellow—one coordinate oxygen atoms, red—two coordinate oxygen atoms and purple—three coordinate oxygen atoms, taken from [34].

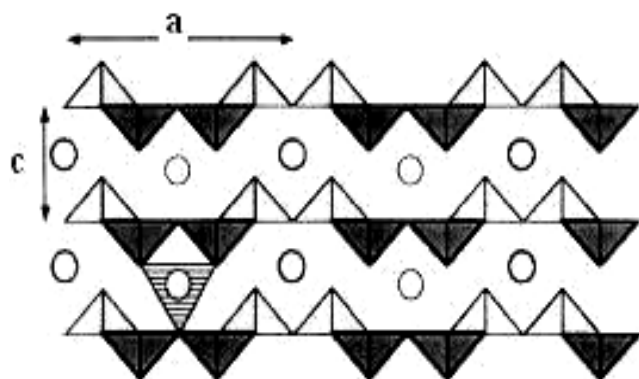


Fig. 4. Presentation of the α -phase. Triangles present VO_5 square pyramids and circles M (= e.g. lithium) atoms, taken from [35].

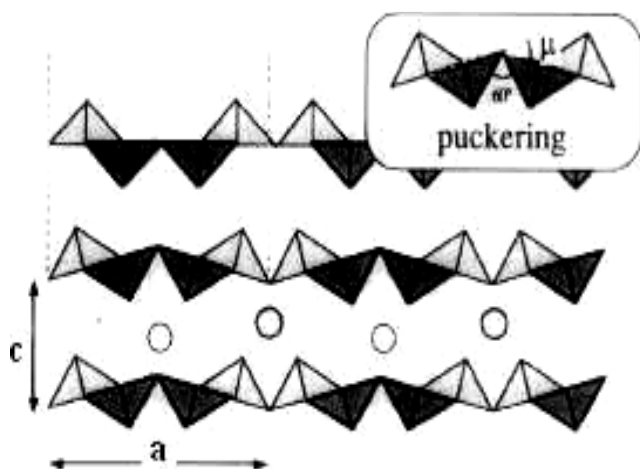


Fig. 5. Puckering of V_2O_5 layers, taken from [35].

Depending on the amount of the inserted lithium several structures were observed: α -phase exists for a small amount of lithium $x < 0.01$ being introduced between the layers on sites, which can be described as trigonal prisms (see **Fig. 4**).

In addition, ϵ -phase forms for $0.35 < x < 0.7$ in $Li_xV_2O_5$. Both phases exhibit a V_2O_5 -type structure with increasing puckering of the layers [36]. Maximum puckering occurs when the puckering angle of the basal oxygen plane (μ) is raised at an angle of 60° . Ideally, μ varies from 0° up to 30° for V_2O_5 (see **Fig. 5**).

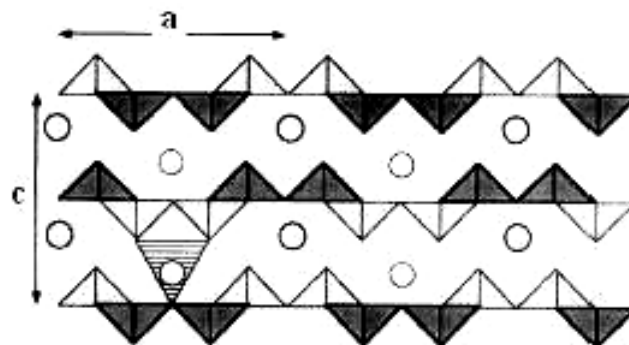


Fig. 6. Presentation of the δ -phase. Lithium atoms are tetrahedrally surrounded, taken from [35].

For the composition LiV_2O_5 gliding of one layer out of two, leads to the δ -phase (see **Fig. 6**). This layered structure has been determined by Cava et al. [37]. It consists of $[V_2O_5]_n$ layers of the V_2O_5 type, alternatively shifted by $b/2$ along $[010]$. This implies a doubling of the c parameter.

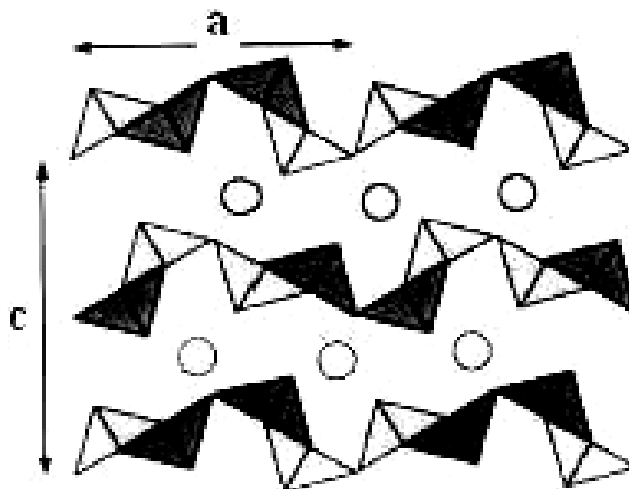


Fig. 7. Presentation of the γ -phase. The lithium between layers is octahedrally surrounded by oxygen, taken from [35].

All the phase transitions are fully reversible and the pristine V_2O_5 phase is recovered upon lithium extraction. However, for lithium content $x > 1$, the δ -phase is irreversibly transformed via a reconstruction mechanism, leading to a structural modification related to the γ -phase [36] (see **Fig. 7**). It was shown in 1989 that the resulting γ -phase can be reversibly cycled in the stoichiometric range $0 < x < 2$ under retention of the γ -type structure [38]. This structure exhibits puckered $[V_2O_5]_n$ layers in which the electronic localization has been established. Thus, two $[V^{+5}O_5]$ and $[V^{+4}O_5]$ square pyramids of widely different sizes were observed [35].

Further insertion of a third lithium into V_2O_5 leads to the irreversible formation of the so-called ω -phase with a rock-salt type structure. The resulted compound

demonstrated a specific energy up to 900 Wh kg^{-1} and 100 cycles with more than 450 Wh kg^{-1} cell in a voltage range between 3.4 and 1.9 V. Thus, it showed great potential as a cathode material for lithium batteries, which has been demonstrated for a $\omega\text{-Li}_x\text{V}_2\text{O}_5/\text{Li}$.

2.2. $\text{V}_2\text{O}_5 \cdot n\text{H}_2\text{O}$ gels

Besides V_2O_5 , promising results have also been reported for $\text{V}_2\text{O}_5 \cdot n\text{H}_2\text{O}$ xerogels (see Fig. 8). These structures offer considerable advantages due to their morphology. A large electrochemically active surface area, small particle size, and low density provide both high overall diffusion coefficients and low volume expansion during lithium intercalation [2]. Specific energies of over 700 Wh kg^{-1} were measured for lithium cells with a xerogel cathode [39]. However, limited long-term cycling stability is a major problem of such cathode materials at present.

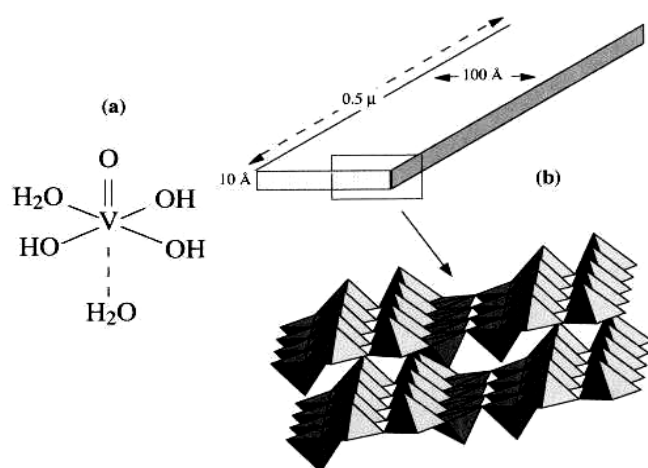


Fig. 8. Structure of $\text{V}_2\text{O}_5 \cdot n\text{H}_2\text{O}$ gels, taken from [40].

Despite decades of experimentation with $\text{V}_2\text{O}_5 \cdot n\text{H}_2\text{O}$, its atomic structure has remained a mystery because it does not form crystals and exists only as ribbonlike particles about 10 nm wide and $1 \mu\text{m}$ long [41]. Livage et al. proposed that the xerogel, on the atomic scale, is a stack of corrugated single layers of VO_5 units having a step of $\approx 2.9 \text{ \AA}$, with the layers closely related to those occurring in crystalline V_2O_5 [41]. On the other hand, Oka et al. proposed that $\text{V}_2\text{O}_5 \cdot n\text{H}_2\text{O}$ is made of V_2O_5 bilayers according to the crystalline structure of $\text{A}_x\text{V}_2\text{O}_5$ ($\text{A}=\text{Na}, \text{K}$) [42]. This model is further supported by polarised X-ray absorption and XAFS studies on deposited $\text{V}_2\text{O}_5 \cdot n\text{H}_2\text{O}$ films [43].

The structure of $\text{V}_2\text{O}_5 \cdot n\text{H}_2\text{O}$ xerogel has been determined for the first time using the atomic pair distribution function (PDF) technique [18] (see Fig. 9). The structure differs from that of crystalline V_2O_5 and is consistent with the one proposed by Oka et al. At the atomic scale, the xerogel can be well described as a double layer of V_2O_5 stacked along the c -axis of a monoclinic unit cell. The stacking sequence is imperfect, confirming the widespread view of the extensive turbostratic disorder in this system. The closest distance between the bilayers is about 11.5 \AA . When the xerogel intercalates or extracts guest species, this distance expands or contracts correspondingly. While, the distance

between the two single sheets of V_2O_5 making up the bilayer slab is approximately 2.90 \AA [2] (see Fig. 9).

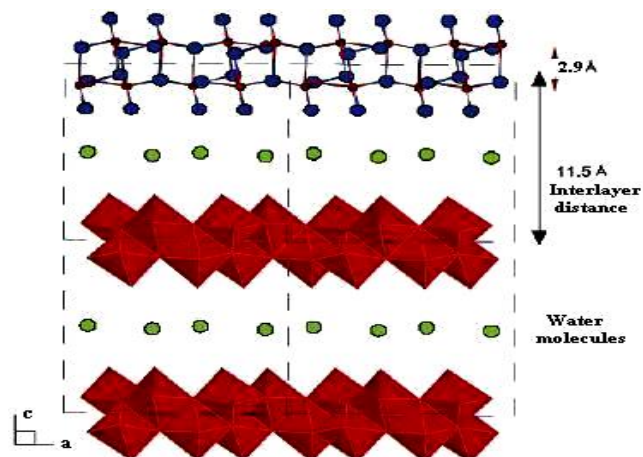
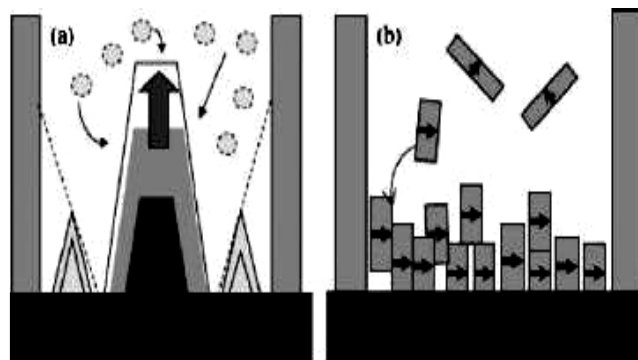


Fig. 9. Taken from [18] Structure of $\text{V}_2\text{O}_5 \cdot n\text{H}_2\text{O}$ xerogel as revealed by PDF analysis. Water molecules are shown in green.



Scheme 1. Schematic illustrations of growth mechanisms of single crystalline nanorods: (a) evolution selection growth, and (b) homoepitaxial aggregation, taken from [44].

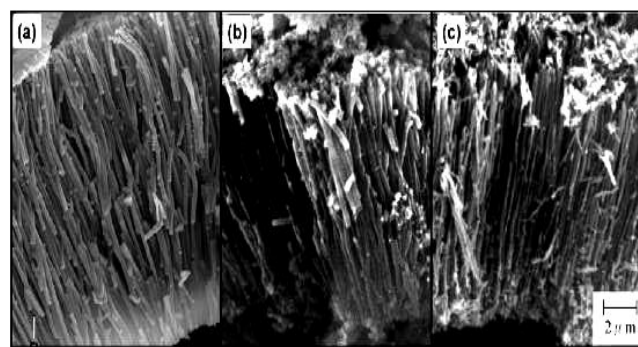


Fig. 10. SEM images of V_2O_5 nanorods grown in a PC membrane with 200 nm diameter pores: (a) from VOSO_4 solution, (b) from $[\text{VO}_2^+]$ solution with pH change, and (c) from the sol-gel route grown on a positive electrode, taken from [44].

3. Vanadium pentoxide nanostructures as Lithium battery electrodes

3.1. Nanorod arrays

Synthesis and electrochemical properties of single-crystal V_2O_5 nanorod arrays were first reported by Cao, Wang and

co-workers. They have utilized a template-based electrodeposition method by depositing V_2O_5 into pores of polycarbonate (PC) templates, with the assistance of electric field from three different types of solution (see Fig. 10). The formation of single-crystal nanorods from solutions by electrochemical deposition is attributed to evolution selection growth (Scheme 1 (a)). While, in the case of nanorods made from the V_2O_5 sol by electrophoretic deposition, the formation of single-crystal nanorods is explained by homoepitaxial aggregation of crystalline nanoparticles (Scheme 1 (b)).

Patrissi and Martin deposited triisopropoxyvanadium (V) oxide into the pores of polycarbonate using the template synthesis by removal of membranes at high temperature to form orthorhombic V_2O_5 nanorod arrays [16]. They found that the arrays deliver three times the capacity of the thin film electrode. After that, Li et. al. achieved improved volumetric energy densities of V_2O_5 nanorod arrays by chemically etching the polycarbonate membrane to increase its porosity prior to template synthesis [45]. Sides and Martin prepared V_2O_5 nanorods of different diameters at low temperature to compare their electrochemical properties. They investigate that the V_2O_5 nanorods with a diameter of 70 nm deliver higher specific discharge capacities than those with micrometer-sized diameters [46]. Fig. 11 shows the comparison between the current density and lithium ion intercalation capacity of nanorod arrays and sol-gel films measured by chronopotentiograms (CPs).

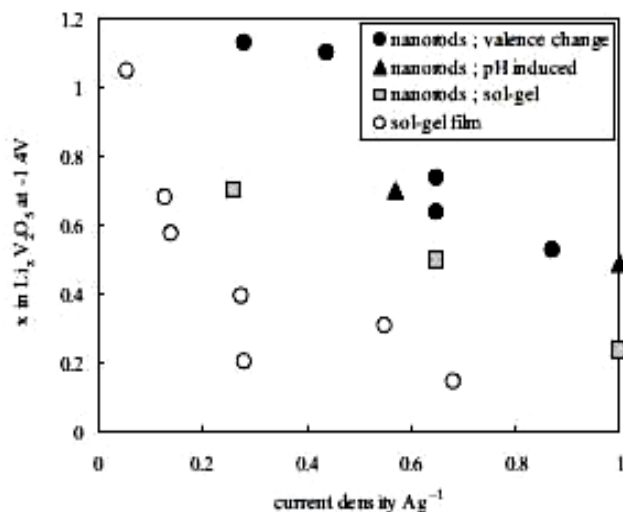


Fig. 11. Discharge capacity versus current density for V_2O_5 nanorod arrays and sol-gel derived films, taken from [44].

It is shown that for a given lithium ion intercalation capacity, nanorod arrays from solution route possess an up to five times larger current density than that of sol-gel films, which is larger than that of the sol electrophoresis nanorod. Similarly for a given current density, such as $0.7 Ag^{-1}$, nanorod arrays can store up to five times more Li than in sol-gel films and more than in the sol electrophoresis nanorod. The differences in their electrochemical properties are attributed to the differences in the size of the structures. Nanorods grown by electrochemical deposition from solutions are dense single crystals, with layers parallel to the nanorod axis. This structure is favourable to lithium ion intercalation and extraction, because the surface oxidation

and reduction reactions occur along the surface of the nanorods and the solid-state diffusion distance is very small [14]. In addition, such structure permits the most freedom for dimensional change that accompanies intercalation and extraction reactions. The nanorod grown from sol electrophoresis is also single-crystalline and well-aligned, but it has many defects inside the crystal, which may cause the difference between these nanorod array electrodes.

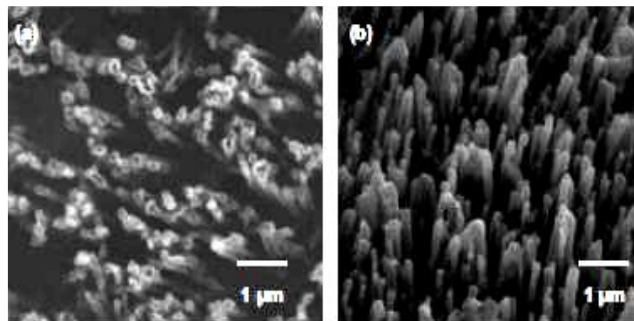


Fig. 12. (a) Top- and (b) side-view SEM images of electrochemically deposited V_2O_5 nanotubes within 200 nm diameter pores of a polycarbonate membrane after the membrane was dissolved away in methylene chloride, taken from [48].

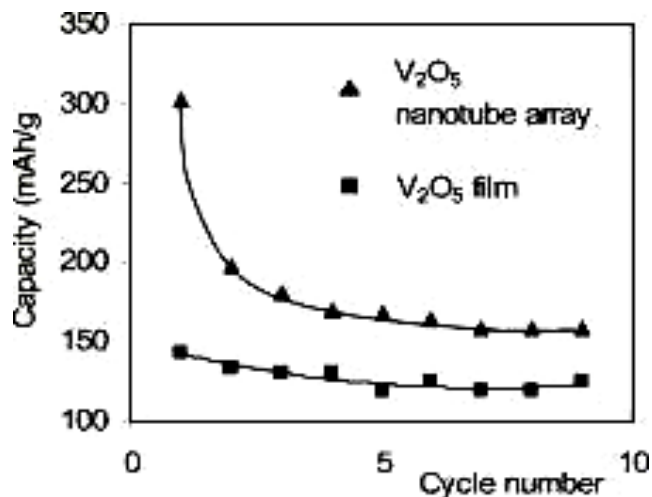


Fig. 13. Dependence of the discharge capacity on the cycle number obtained from chronopotentiometric measurements at a cut off voltage of 0.4 to $-1.5 V$ versus Ag/Ag , taken from [49].

3.2. Nanotube arrays

The first successful approach to make vanadium oxide nanotubes was carried out using the carbon nanotubes as a template. It was possible by exploitation of surface-tension effects to coat the carbon nanotubes externally with crystalline layers of a V_2O_5 -like structure [47]. Nanotube arrays of $V_2O_5 \cdot nH_2O$ have also been prepared through the template-based electrodeposition method from $[VO_2^+]$ solution by using lower voltage and shorter deposition time compared to the conditions for preparing nanorod arrays [48]. Upon completion of deposition, the sample was dried at $110^\circ C$ for 6 h and was then attached to an indium tin oxide (ITO) substrate with silver paste (Ted Pella Inc.). The as-prepared sample on the ITO substrate was dried at $110^\circ C$ for another 6 h and was immersed in methylene chloride to dissolve the polycarbonate membrane, resulting

in an ensemble of $V_2O_5 \cdot nH_2O$ nanotubes on an ITO substrate. **Fig. 12** shows top- and side-view SEM images of a V_2O_5 nanotube array grown within the pores of a polycarbonate membrane after the membrane was dissolved away in methylene chloride.

The $V_2O_5 \cdot nH_2O$ nanotube arrays demonstrate an initial high capacity of 300 mAh g^{-1} , about twice the initial capacity of 140 mAh g^{-1} from the $V_2O_5 \cdot nH_2O$ film (see **Fig. 13**).

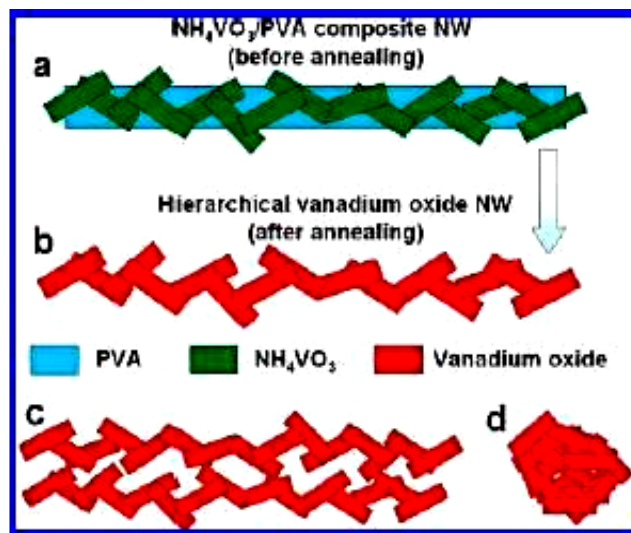
Such enhancement of capacity is due to the large surface area and short diffusion distances offered by the nanotube array [14]. However, degradation was observed during the electrochemical characterization of the arrays, which is slower after the third cycle. In addition, the capacity stabilizes at 160 mAh g^{-1} after the sixth cycle, which is about 30 % higher than the stabilized capacity of the $V_2O_5 \cdot nH_2O$ film. The initial degradation of the $V_2O_5 \cdot nH_2O$ film suggests that $V_2O_5 \cdot nH_2O$ itself prepared from electrochemical deposition has some drawback and suffers a slight loss in electroactivity during cycling. However, the nanotube array shows a more drastic decay of initial performance compared to the film during cycling, possibly due to the morphological flexibility and fragility of the nanotubes, which has also been speculated in the literature [49].

3.3. Nanowires

Pan et al. used a hydrothermal method to synthesize long beltlike nanowires, which are several tens of micrometers long and a few tens of nanometers wide [50]. A hydrothermal method was also later used by Schlecht et al. to synthesize new types of vanadium oxide belts exhibiting a boomerang shape [51]. A layered structure was revealed closely corresponding to vanadium pentoxide nanofibers. The structure of nanobelts is unique in that it originates from twinning along the [130] direction, which is the first observation of twins within individual nanosized crystals. However, the intercalation properties of these beltlike nanowires or boomerang-shaped nanobelts of vanadium oxides were not further investigated. Chang et al. recently reported growth conditions of V_2O_5 nanowires and demonstrated a simple but noble percolation system composed of the conducting nanowires and insulating matrix [52]. They are prepared from ammonium metavanadate with acidic ion-exchange resin. The length of V_2O_5 is controlled by keeping the mixture of ammonium metavanadate and acidic ion-exchange resin for a certain time period. Longer aging time leads to longer V_2O_5 nanowires in the sol, for example, nanowires of a few micrometers long are obtained by keeping the mixture for 20 days. This procedure produced a brown sheet, which is rinsed with water and then peeled off the filter paper, resulting in a free-standing sheet composed of entangled V_2O_5 nanowires. Gu et al. also demonstrated the growth of V_2O_5 nanowires using a method similar with Chang et al. for electrochemical actuators [53].

Furthermore, ultralong hierarchical vanadium oxide nanowires can be formed using the following procedure: as NH_4VO_3 /PVA solution jet accelerated toward the grounded aluminium foil, then NH_4VO_3 crystals began to grow accompanied by rapid evaporation of solvent. Meanwhile, the PVA nanowire played the role of a template for the

oriented growth of attached NH_4VO_3 nanorods, which resulted in the formation of ultralong hierarchical NH_4VO_3 /PVA composite nanowires, as illustrated in Scheme 2 a. Finally, the ultralong hierarchical vanadium oxide nanowires made up of attached nanorods were formed after annealing, as illustrated in **Scheme 2 b**.



Scheme 2. (a, b) Schematic illustration of formation of the ultralong hierarchical vanadium oxide nanowires during annealing. (c) Side view of two ultralong hierarchical vanadium oxide nanowires near each other. (d) Self-aggregation of short vanadium oxide nanorods, taken from [54].

This novel nanostructure exhibits high performance for lithium ion batteries, providing a high discharge capacity of 390 mAh g^{-1} and improved cycling stability, which results from reduced self-aggregation of the nanomaterials [54].

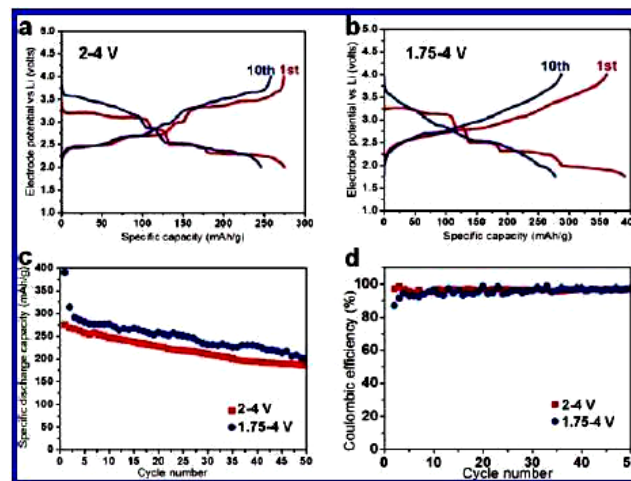


Fig. 14. (a, b) Charge/discharge curves of hierarchical vanadium oxide nanowires at 2-4 and 1.75-4 V, respectively. (c, d) Capacity vs. cycle number, and Coulombic efficiency vs. cycle number of the ultralong hierarchical vanadium oxide nanowires, taken from [54].

3.4. Nanorolls and nanobelts

Pioneering work on the synthesis and electrochemical properties of vanadium oxide nanorolls has been carried out by Spahr and co-workers [55]. In their synthesis, a combination of sol-gel reaction and hydrothermal treatment

of vanadium oxide precursor is conducted in the presence of structure-directing template. The resultant nanoroll is either constructed in closed concentric cylinders (nanotubes) or formed by scrolling one or more layers (nanoscrolls). If amine is replaced by ammonia during the hydrolysis step, a new type of vanadium oxide nanoroll (nanotube) with alternating interlayer distances is yielded [56]. Such a unique structure is first observed in a tubular phase. Compared to other tubular systems, the vanadium oxide nanorolls are especially interesting because they possess four different contact regions, that is, tube opening, outer surface, inner surface, and interstitial region.

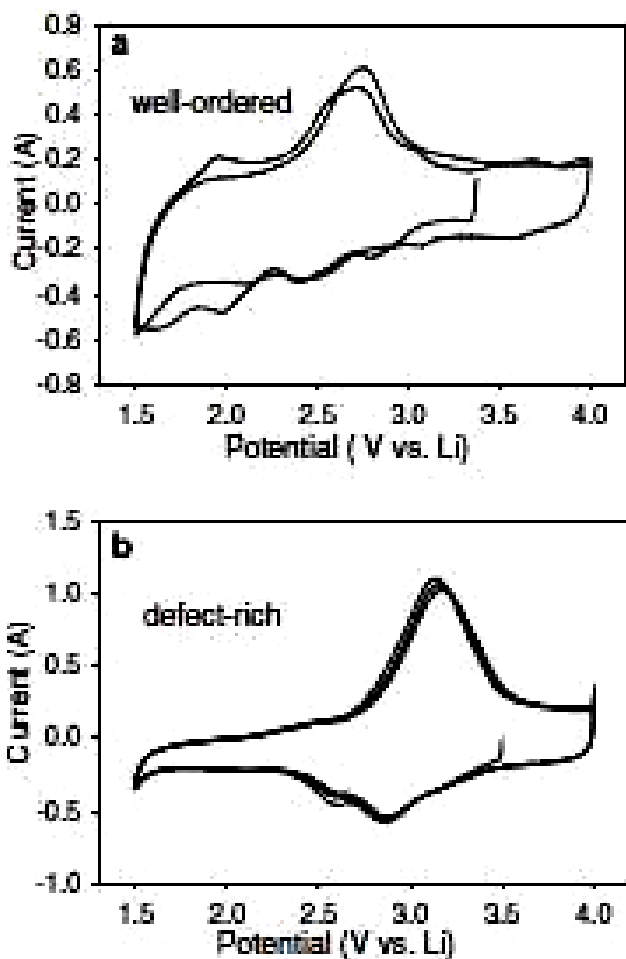


Fig. 15. Cyclic voltammograms for Na-exchanged vanadia nanorolls (30 min exchange time) a) well-ordered vanadium oxide nanorolls, and b) defect-rich nanorolls. The well-ordered material shows many steps in the CV curves, similar to crystalline layered vanadates. By contrast, the CV curves for the defect-rich nanorolls are quite similar to sol-gel prepared vanadia, taken from [57].

The relationship between the nanoscale structure and the electrochemical properties of vanadium oxide nanorolls has been demonstrated by Sun et al. [57]. The well-ordered nanorolls behave similarly to classic crystalline vanadium oxides, while the defect-rich materials behave more closely to sol-gel vanadium oxides, which are only partly crystalline on the atomic scale (see Fig. 15). The combination of nanoscale and atomic scale disorder appears to produce the highly desirable combination of increased specific capacity and better cyclability. It is proposed that the increased capacity is associated with

additional redox sites that result from the atomic scale disorder. While the better cycle lifetimes are associated with increased accessibility of alkali ions to the gallery regions between the layers because of the cracks and exfoliations in the defect-rich nanotubes.

Li et al. have studied the synthesis and electrochemical behaviour of orthorhombic single-crystalline V_2O_5 nanobelts [58]. The V_2O_5 nanobelts with widths of 100–300 nm, thicknesses of 30–40 nm and lengths up to tens of micrometers are obtained by hydrothermal treatment of aqueous solutions of V_2O_5 and H_2O_2 (see Fig. 16 A). In Fig. 16 B and C, it is found that the belts can be cleaved along the (100) and (001) planes as indicated by the arrows according to Fig. 16 E. The belt-like shape of V_2O_5 is further confirmed by a low-magnification TEM image (see Fig. 16 D). The selected area electron diffraction (SAED) pattern (inset to Fig. 16 D) taken from an individual nanobelt is indexed to orthorhombic V_2O_5 , indicating that a nanobelt is a single crystal, with a preferential growth direction along the [010]. The HRTEM image (see Fig. 16 E) with clear interplanar spacing $d_{020} = 1.78 \text{ \AA}$ and $d_{200} = 5.75 \text{ \AA}$ shows that the belt is structurally perfect and also confirms the growth direction.

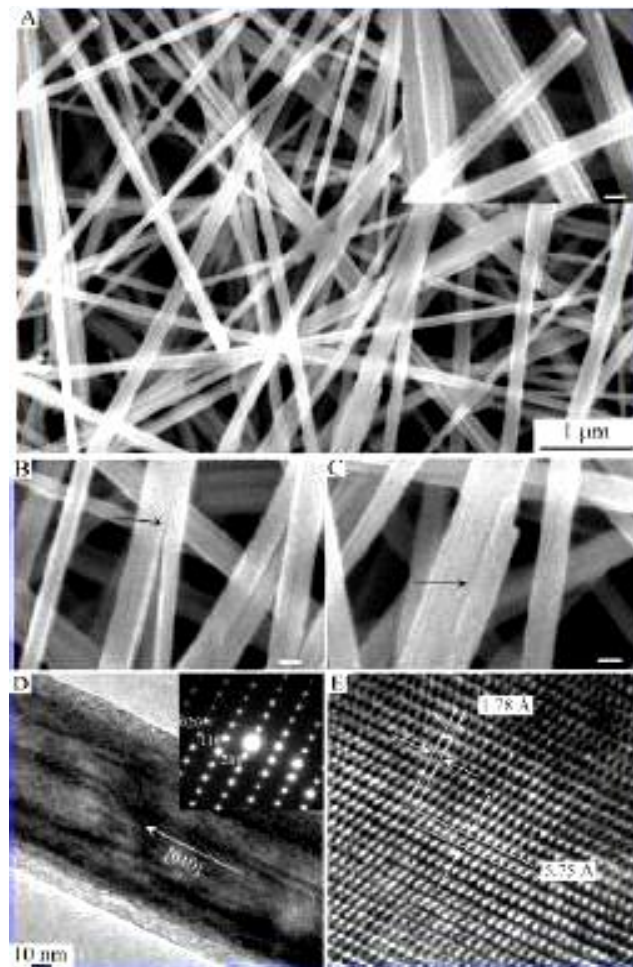


Fig. 16. Taken from [59], SEM (A-C) and TEM (D and E) images of V_2O_5 single crystalline nanobelts synthesized at $180 \text{ }^\circ\text{C}$ for 48 h. The insets to panels A and D show the rectangular cross-section of the belt-like materials and the SAED pattern taken from an individual nanobelt respectively (scale bar = 100 nm).

The discharge curves of the commercial V_2O_5 powders and the as-synthesized V_2O_5 nanobelts are illustrated in **Fig. 17**. In the first circle, the specific discharge capacity of V_2O_5 nanobelts is as high as 288 mAh g^{-1} in the potential range of 1.5–4.0 V, which is much higher than that of commercial V_2O_5 powders (132 mAh g^{-1}) and comparable to that reported by Wan's group (286.4 mAh g^{-1}) [60]. The higher capacity of V_2O_5 nanobelts may be ascribed to their larger specific surface area [59].

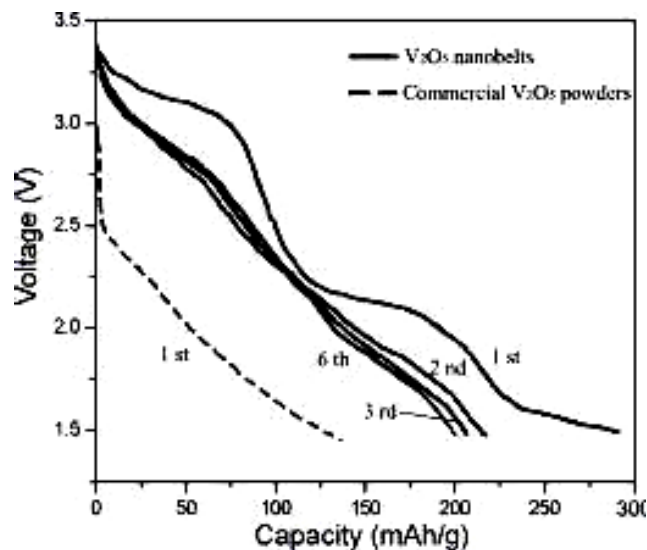
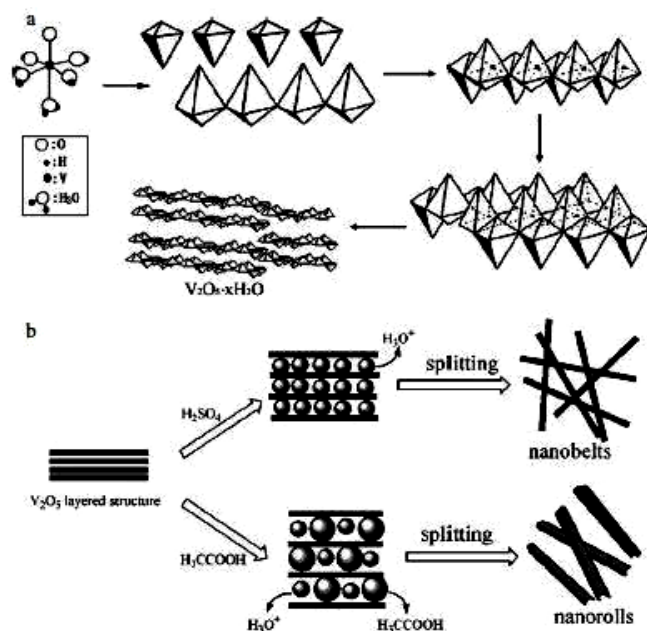


Fig. 17. Taken from [59], Discharge curves of the commercial V_2O_5 powders and the as-synthesized V_2O_5 nanobelts.



Scheme 3. Taken from [60], (a) The formation of layered framework of $V_2O_5 \cdot xH_2O$ by a condensation and polymerization process. (b) The formation of $V_2O_5 \cdot xH_2O$ nanobelts and nanorolls by a H_3O^+ (or CH_3COOH) intercalating or splitting process.

Apart from anhydrous crystalline V_2O_5 , hydrous vanadium pentoxide compounds exhibit electrochemical performance, which is influenced by many factors such as crystallinity, composition, surface area and preparation methods. $V_2O_5 \cdot 0.9H_2O$ nanobelts and ultra-long

$V_2O_5 \cdot 0.6H_2O$ nanorolls with scroll-like structures were successfully synthesized on a large scale by a simple hydrothermal growth method using NH_4VO_3 as the raw material in the presence of sulfuric acid and acetic acid respectively as shown in **Scheme 3**.

In the formation process, neither templates nor surfactants were used in the reaction system. Based on the experimental results of the hydrolysis and condensation of NH_4VO_3 , the H_3O^+ intercalating and splitting process was proposed to elucidate the formation of the 1 D nanostructure in which the acid played the determining role for the formation of nanobelts or nanorolls.

The sample obtained with the dilute sulfuric acid to adjust pH, as shown in **Fig. 18 (a), (b)**, is composed of a large number of uniform nanobelts, 100 – 150 nm wide and 20 – 30 nm thick. **Fig. 18 (c), (d)** display the images of the sample obtained in the presence of dilute acetic acid, indicating that the sample consists of uniform straight wire-like nanostructures with diameters of 100 – 250 nm and length of tens of micrometres. From further observation on **Fig. 18 (d)**, these wire-like nanostructures, were scroll-like nanostructures, i.e. nanorolls, and most of them scroll incompletely to form a kind of half-tube as observed in the inset of **Fig. 18 (d)**.

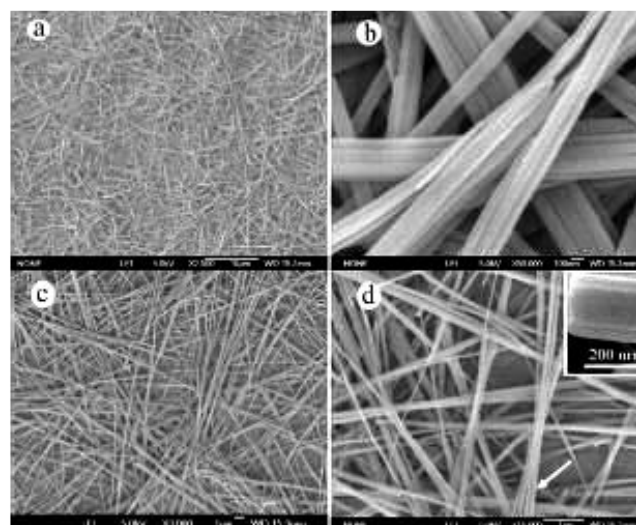


Fig. 18. Taken from [61], FE-SEM images of the obtained $V_2O_5 \cdot xH_2O$ nanobelts and nanorolls. (a), (b) nanobelts obtained using diluted sulfuric acid to adjust pH = 4; (c), (d) nanorolls obtained using diluted acetic acid to adjust pH = 4.

The charge - discharge capabilities of the $V_2O_5 \cdot 0.9H_2O$ nanobelts, $V_2O_5 \cdot 0.6H_2O$ nanorolls and anhydrous V_2O_5 nanostructures were investigated by using the samples as the cathode in a lithium-ion battery as shown in **Fig. 19**. **Fig. 19 (a) and (b)** show a typical charge - discharge curve of crystalline V_2O_5 with a stepwise shape due to the phase change of $Li_xV_2O_5$ during lithium ion intercalation [16]. $V_2O_5 \cdot 0.6H_2O$ nanorolls exhibit a slightly higher initial discharge capacity (253.6 mAh g^{-1}) than $V_2O_5 \cdot 0.9H_2O$ nanobelts (223.9 mAh g^{-1}), which may be attributed to their different morphologies and water contents. In order to investigate the effect of H_2O in crystals on the electrochemical properties of $V_2O_5 \cdot 0.9H_2O$ nanobelts and $V_2O_5 \cdot 0.6H_2O$ nanorolls, the electrochemical properties of the as-obtained anhydrous V_2O_5 nanostructures (sample

500-1 and sample 500-2) were measured under the same conditions, and their charge–discharge profiles in the initial cycle are shown in **Fig. 19 (b)**. The capacitances of samples 500-1 and 500-2 increased to 287.8 mAh g⁻¹ (sample 500-1) and 307.5 mAh g⁻¹ (sample 500-2) demonstrating the significant effect of H₂O on their electrochemical properties. In addition, their cycle performances are shown in **Fig. 19 (c)**, which illustrates the dependence of the discharge capacity on cycle number for these samples. The sample of V₂O₅•0.9H₂O nanobelts and its post-annealing product (sample 500-1) retain nearly 83 % and 74 %, respectively, of their initial discharge capacities after 15 cycles. The capacitance of the V₂O₅•0.6H₂O nanorolls decays relatively fast initially with cycling tests to retain 61 % of its initial discharge capacity after 7 cycles and reaching a stabilized capacitance about 147.0 mAh g⁻¹; the capacitance of its post-annealing product (sample 500-2) decays to retain 67 % of its initial discharge capacity after 15 cycles. The decreasing discharge capacity of the samples is likely due to partial fracture of their shapes and structural degradation after redox cycles.

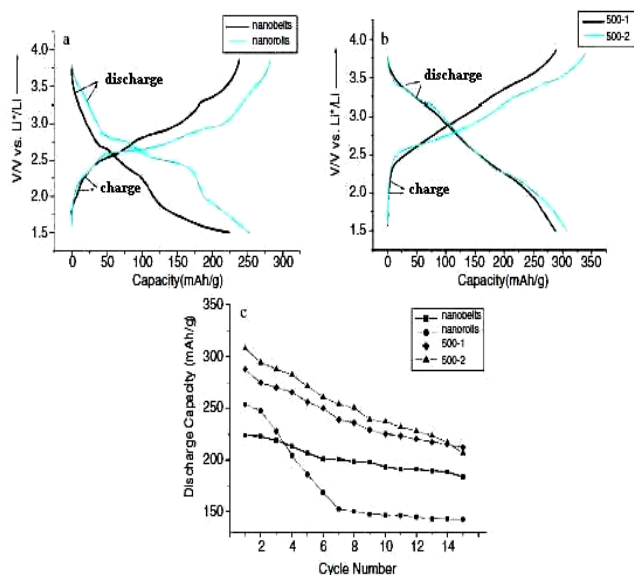


Fig. 19. Taken from [61], (a), (b) Charge–discharge curves in the initial cycle of the as-prepared V₂O₅•xH₂O and anhydrous V₂O₅ nanostructures at a given constant current density of 0.6 mAcm⁻². (c) The cycle performances of capacitances of the V₂O₅•xH₂O and anhydrous V₂O₅ nanostructures.

3.5. Nanoribbons and nanocables

Cui and co-workers prepared V₂O₅ nanoribbons and investigated the dependence of the electrochemical property on the width and thickness of nanoribbons by studying the chemical, structural, and electrical transformations of V₂O₅ nanoribbons at the nanostructured level [62]. They found that transformation of V₂O₅ into the ω-Li₃V₂O₅ phase takes place within 10 s in thin nanoribbons, and the efficient electronic transport can be maintained to charge ω-Li₃V₂O₅ nanoribbon within less than 5 s. Therefore, it is suggested that Li diffusion constant in nanoribbons is faster than that in bulk materials by three orders of magnitude, leading to a remarkable enhancement in power density [63].

Fig. 20 compares the electrochemical performance of Ni-V₂O₅•nH₂O nanocable arrays, single-crystal V₂O₅ nanorod arrays, and sol-gel derived V₂O₅ films. Ni-V₂O₅•nH₂O nanocable arrays demonstrate remarkably improved capacity and rate capability in comparison with the other two. The intercalation capacities of both nanorod arrays and sol-gel films decrease rapidly as the current density increases, while nanocable arrays are able to retain the high capacity at high current density (discharge rate), indicating the excellent high-rate performance of nanocable arrays [64]. In addition, as shown in **Fig. 20 (c)**, Ni-V₂O₅•nH₂O nanocable array has significantly higher energy density and power density than the nanorod array and sol-gel film by at least one order of magnitude, which is ascribed to the enhanced surface area and reduced internal resistance.

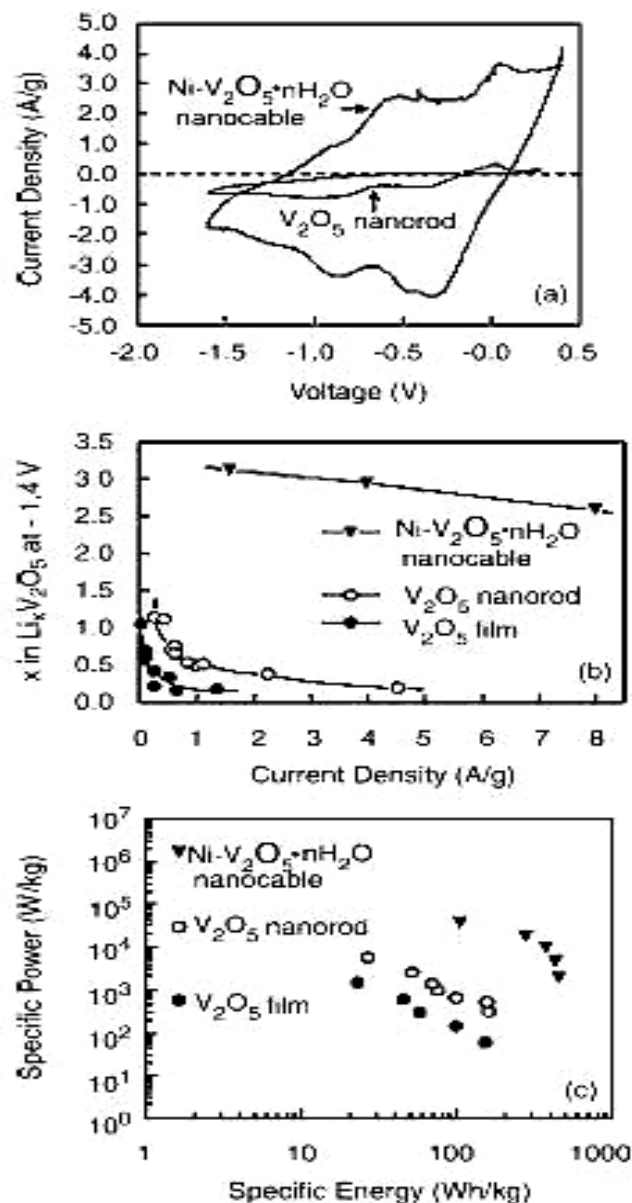


Fig. 20. Taken from [65], a) Cyclic voltammograms of Ni-V₂O₅•nH₂O nanocable array and V₂O₅ nanorod array using a scan rate of 10 mVs⁻¹. b) Relationship between current density and Li intercalation capacity of Ni-V₂O₅•nH₂O nanocable array, V₂O₅ nanorod array and sol-gel film from chronopotentiometric measurements. c) Ragone plot for Ni-V₂O₅•nH₂O nanocable array, V₂O₅ nanorod array and sol-gel film.

3.6. Gels

Nanocomposites of vanadium oxide aerogel with single-walled carbon nanotubes (SWNT) were prepared by integrating the nanotubes as part of the sol-gel chemistry. The nanocomposite electrodes were prepared by mixing the V_2O_5 -SWNT powder with poly(vinylidene fluoride) in cyclohexane to form slurry, which was then applied to a stainless steel mesh [66]. For comparison, traditional electrodes were prepared using carbon black (CB) powder as the conductive additive. The voltammetric responses for the aerogel immobilized on the sticky carbon electrode are shown in **Fig. 21**. In the $LiClO_4$ /propylene carbonate (PC) electrolyte, a broad and capacitive response is observed, and the intercalation peaks appear to be superimposed upon the capacitive response (**Fig. 21a**). The background from the sticky carbon electrode is negligible. At high scan rates, the aerogel responds as a conventional capacitor (**Fig. 21b**). In contrast, when the same V_2O_5 aerogel is prepared in a conventional electrode structure, as a composite with carbon additive and binder, the characteristic intercalation behaviour for sol-gel derived V_2O_5 materials is observed (**Fig. 21c**). Finally, electrochemical measurements which were made using an electrolyte of tetrabutyl ammonium perchlorate (TBAP) dissolved in PC show very different behaviours (**Fig. 21d**). In this case, the response for the aerogel immobilized on the sticky carbon is significantly less than that obtained in the Li^+ electrolyte.

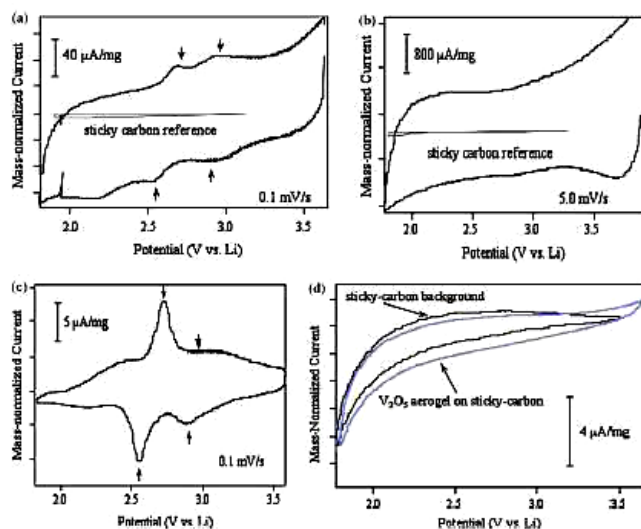


Fig. 21. Taken from [67], voltammetric response of V_2O_5 aerogel on sticky carbon in $LiClO_4$ /PC electrolyte at (a) 0.1 mVs^{-1} and (b) 5 mVs^{-1} . The sticky carbon response is also shown. Voltammetric response of a typical composite electrode at (c) 0.1 mVs^{-1} . Voltammetric response of the aerogel on sticky carbon in TBAP electrolyte (d).

The specific capacitance and the lithium capacity for the various samples are shown in **Table 1**. The lithium capacity value (400 mAhg^{-1}) is nearly three times larger than the lithium capacity of a traditional positive electrode material such as $LiCoO_2$ [6]. Such large energy density shows the benefit of working with electrochemical systems, which exhibit more than one electron redox reactions. The specific capacitance values range from 960 Fg^{-1} to over 2000 Fg^{-1} depending upon the drying method, supercritical or ambient. The largest specific capacitance, 2300 Fg^{-1} , was

obtained using cyclohexane as the drying solvent and corresponds to nearly 1500 mFcm^{-2} . Such a large magnitude of specific capacitance arises from pseudocapacitive behaviour [68], which is a very different charge storage mechanism than that which occurs with traditional intercalation materials [69].

In addition, the data summarized in **Table 1** indicate how the aerogel morphology influences electrochemical properties. Supercritically dried aerogels have high surface areas, but include many nanosized pores of less than 5 nm. These small pores may not be readily accessible to the electrolyte and, in that case, their contribution to the sample capacitance will be nominal. In contrast, samples dried with a low surface tension solvent at ambient pressure tend to have larger pores, in the range of 10 to 30 nm. The significant level of pore volume in combination with larger size pores greatly improves the likelihood that electrolyte penetration occurs throughout the entire particle.

Table 1. A comparison of V_2O_5 aerogels and ambigels shows how specific capacitance depends on the surface area and percentage porosity, taken from [67].

Drying solvent	Specific capacitance (F/g)	Specific capacitance (μFcm^{-2})	Lithium capacity (mAh/g)	Surface area (m^2/g)	% porosity	Total pore volume (cm^3/g)
Supercritical CO_2	1200	430	500	280	98	0.50
Ethylene	1280	640	450	300	86	0.60
Pentane	960	520	400	185	89	0.48
Cyclohexane	2300	1480	650	155	84	0.87
Supercritical CO_2 using TBA	140	45	100	280	98	0.50

4. Electrochromic properties of vanadium pentoxide nanostructures

Fig. 22 shows the change of transmittance intensity at 700 nm as a function of time when an external voltage of 3.0 V is applied for the V_2O_5 nanorod array grown by electrophoretic deposition from the sol and the sol-gel derived V_2O_5 film, respectively.

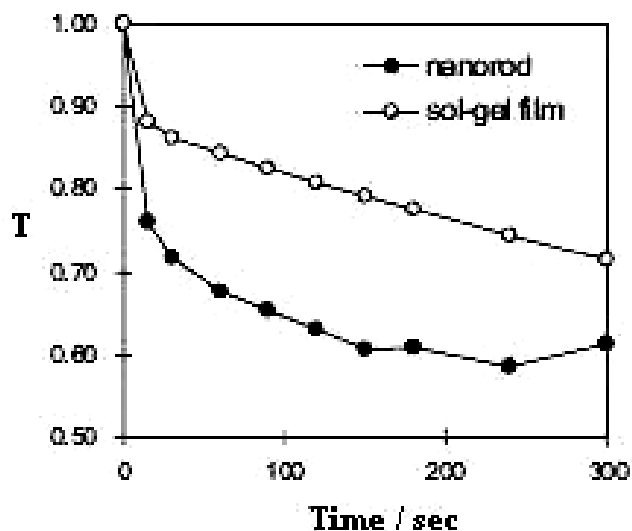


Fig. 22. Taken from [70], transmittance intensity of nanorod arrays and sol-gel films subjected to an externally applied electric field as a function of time.

A 30 % reduction was achieved in ca. 50 s in the V_2O_5 nanorod array; however, 300 s were required in the film. In conclusion, both the extent and the speed of change in the

transmittance intensity of the nanorod array are significantly faster than those of the sol-gel derived film, corroborating with an enhanced electrochemical intercalation process in nanorod arrays due to a large surface area for the surface redox reaction and a short and easy diffusion path for mass and charge transport [14].

When a suitable potential is applied for 30 s for each step, the coloration and bleaching states of V_2O_5 nanowire-based electrochromic device are pale blue and yellow, respectively (see Fig. 23), and the maximum transparent contrast ΔT is 37.4 % at $\lambda = 415$ nm.

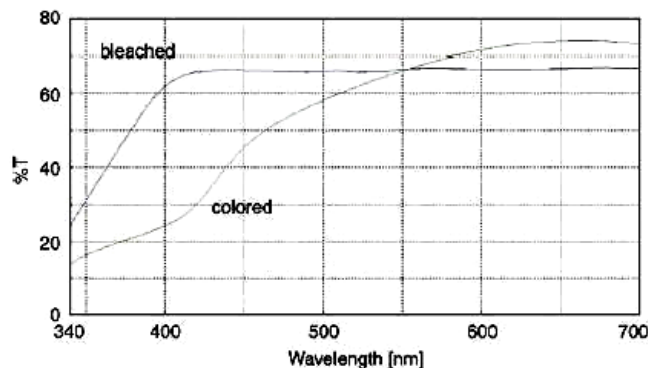


Fig. 23. Taken from [71], transmittance spectrum of the colored (+1 V) and bleached (-1 V) states of the V_2O_5 nanowires in the range of 340 – 700 nm.

Using the same conditions, the switching speed is measured from time dependence of transmittance responses as shown in Fig. 24. The switching time is found to be about 6 s from colored state (+1 V) to bleached state (-1 V) and 5 s from bleached state (-1 V) to colored state (+1 V).

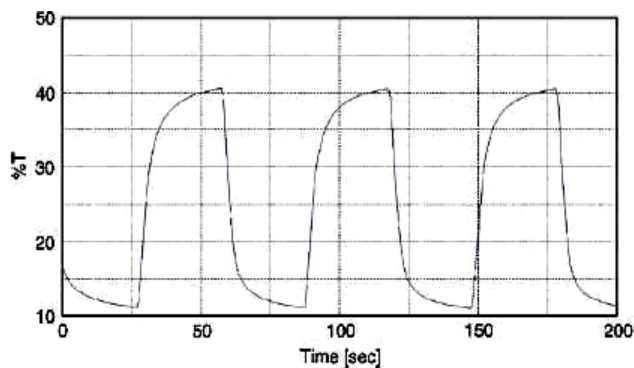


Fig. 24. Taken from [71], transmittance spectrum of the V_2O_5 nanowires at 415 nm as a function of time upon potential switching between +1 and -1 V.

Conclusion

In this paper, a review on the lithium intercalation properties of vanadium pentoxide nanostructures is presented. The morphology and the structure of nanorod arrays, nanotube arrays, nanowires, anhydrous and hydrous nanorolls and nanobelts, nanoribbons, nanocables and gels have been discussed. Their intercalation properties have been investigated and compared to those of the vanadium pentoxide film electrodes. It is demonstrated that the nanostructured electrodes exhibit enhanced storage capacity and rate performance over those of V_2O_5 films. In

particular, the $Ni-V_2O_5 \cdot nH_2O$ nanocable array presents higher energy density and power density than the nanorod array due to the enhanced surface area and the reduced internal resistance. Further, the electrochemical characterizations of the anhydrous vanadium pentoxide nanorolls and nanobelts have demonstrated higher discharge capacity and more sustainable cycling life than the hydrous nanostructures. Finally, it is shown that both the extent and the speed of change in the transmittance intensity of the nanorod array are significantly faster than those of the sol-gel derived film. There is much chemistry still remaining to fully understand the intercalation properties of vanadium pentoxide nanostructures with respect to lithium and other cations. On the other hand, there is a lot of research work to go related with the opportunities of the nanostructures as electrochromics. The vanadium pentoxide nanostructures will continue their ongoing improvement with further decreasing their size offering enhanced electrochemical performance at a low growth cost. However, the low cost of the lithium batteries and the electrochromics will only be achieved if the costs of the other components such as anodes, transparent conducting materials and electrolytes are also reduced. This can possibly be achieved using carbon related materials and solid instead of liquid electrolytes.

Reference

- Cheng, F.; Chen, J. *J. Mater. Chem.* **2011**, *21*, 9841. DOI: [10.1039/C0JM04239K](https://doi.org/10.1039/C0JM04239K)
- Wang, Y.; Cao, G. *Chem. Mater.* **2006**, *18*, 2787. DOI: [10.1021/cm052765h](https://doi.org/10.1021/cm052765h)
- Chernova, N.A.; Roppolo, M.; Dillon, A.C.; Whittingham, M.S. *J. Mater. Chem.* **2009**, *19*, 2526. DOI: [10.1039/B819629J](https://doi.org/10.1039/B819629J)
- Granqvist, C.G.; Azens, A.; Hjelm, A.; Kullman, L.; Niklasson, G.A.; Rönnow, D.; Strømme Mattsson, M.; Veszelei, M.; Vaivars, G. *Sol. Energy* **1998**, *63*, 199. DOI: [10.1016/S0038-092X\(98\)00074-7](https://doi.org/10.1016/S0038-092X(98)00074-7)
- Winter, M.; Brodd, R.J. *Chem. Rev.* **2004**, *104*, 4245. DOI: [10.1021/cr020730k](https://doi.org/10.1021/cr020730k)
- Winter, M.; Besenhard, J.O.; Spahr, M.E.; Novák, P. *Adv. Mater.* **1998**, *10*, 725. DOI: [10.1002/\(SICI\)1521-4095\(199807\)10:10<725::AID-ADMA725>3.0.CO;2-Z](https://doi.org/10.1002/(SICI)1521-4095(199807)10:10<725::AID-ADMA725>3.0.CO;2-Z)
- Bazito, F.F.C.; Torresi, M.R. *J. Braz. Chem. Soc.* **2006**, *17*, 627. DOI: [10.1590/S0103-50532006000400002](https://doi.org/10.1590/S0103-50532006000400002)
- Kumta, P.N.; Gallet, D.; Waghay, A.; Blomgren, G.E.; Setter, M.P. *J. Power Sources* **1998**, *72*, 91. DOI: [10.1016/S0378-7753\(97\)02680-3](https://doi.org/10.1016/S0378-7753(97)02680-3)
- Ohzuku, T.; Ueda, A. *Solid State Ionics* **1994**, *69*, 201. DOI: [10.1016/0167-2738\(94\)90410-3](https://doi.org/10.1016/0167-2738(94)90410-3)
- Ohzuku, T.; Ueda, A.; Nagayama, N. *J. Electrochem. Soc.* **1993**, *140*, 1862. DOI: [10.1149/1.2220730](https://doi.org/10.1149/1.2220730)
- Dahn, J.R.; von Sacken, U.; Michal, C.A. *Solid State Ionics* **1990**, *44*, 87. DOI: [10.1016/0167-2738\(90\)90049-W](https://doi.org/10.1016/0167-2738(90)90049-W)
- Abello, L.; Husson, E.; Repelin, Y.R.; Lucazeau, G. *Spectrochim. Acta* **1983**, *39*, 641. DOI: [10.1016/0584-8539\(83\)80040-3](https://doi.org/10.1016/0584-8539(83)80040-3)
- Thackeray, M.M. *J. Electrochem. Soc.* **1995**, *142*, 2558. DOI: [10.1149/1.2050053](https://doi.org/10.1149/1.2050053)
- Wang, Y.; Takahashi, K.; Lee, K.; Cao, G. *Adv. Funct. Mater.* **2006**, *16*, 1133. DOI: [10.1002/adfm.200500662](https://doi.org/10.1002/adfm.200500662)
- Portiron, E.; Salle, A.L.; Varbaere, A.; Piffard, Y.; Guyomard, D. *Electrochim. Acta* **1999**, *44*, 197. DOI: [10.1016/S0013-4686\(99\)00204-2](https://doi.org/10.1016/S0013-4686(99)00204-2)
- Patrissi, C.J.; Martin, C.R. *J. Electrochem. Soc.* **1999**, *146*, 3176. DOI: [10.1149/1.1392451](https://doi.org/10.1149/1.1392451)

17. Takahashi, K.; Limmer, S.J.; Wang, Y.; Cao, G.Z. *J. Phys. Chem. B* **2004**, *108*, 9795.
DOI: [10.1021/jp0491820](https://doi.org/10.1021/jp0491820)
18. Petkov, V.; Trikalitis, P.N.; Bozin, E.S.; Billinge, S.J.L.; Vogt, T.; Kanatzidis, M.G. *J. Am. Chem. Soc.* **2002**, *124*, 10157.
DOI: [10.1021/ja026143y](https://doi.org/10.1021/ja026143y)
19. Artuso, F.; Bonino, F.; Decker, F.; Lourenco, A.; Masetti, E. *Electrochim. Acta* **2002**, *47*, 2231.
DOI: [10.1016/S0013-4686\(02\)00061-0](https://doi.org/10.1016/S0013-4686(02)00061-0)
20. Varsano, F.; Decker, F.; Masetti, E.; Croce, F. *Electrochim. Acta* **2001**, *46*, 2069.
DOI: [10.1016/S0013-4686\(01\)00408-X](https://doi.org/10.1016/S0013-4686(01)00408-X)
21. Owens, B.B.; Passerini, S.; Smyrl, W.H. *Electrochim. Acta* **1999**, *44*, 215.
DOI: [10.1016/S0013-4686\(99\)00205-4](https://doi.org/10.1016/S0013-4686(99)00205-4)
22. <http://home.howstuffworks.com/home-improvement/construction/green/smart-window4.htm>
23. Colton, R.J.; Guzman, A.M.; Rabalais, I.W. *J. Appl. Phys.* **1978**, *49*, 409.
DOI: [10.1063/1.324349](https://doi.org/10.1063/1.324349)
24. Andersson, A.M.; Granqvist, C.G.; Stevens, J.R. *Appl. Opt.* **1989**, *28*, 3295.
DOI: [10.1364/AO.28.003295](https://doi.org/10.1364/AO.28.003295)
25. Cogan, F.; Nguyen, N.M.; Perrotti, S.I.; Rauh, R.D. *J. Appl. Phys.* **1989**, *66*, 1333.
DOI: [10.1063/1.344432](https://doi.org/10.1063/1.344432)
26. Talledo, A.; Andersson, A.M.; Granqvist, C.G. *J. Mater. Res.* **1990**, *5*, 1253.
DOI: [10.1557/JMR.1990.1253](https://doi.org/10.1557/JMR.1990.1253)
27. Talledo, A.; Andersson, A.M.; Granqvist, C.G. *J. Appl. Phys.* **1991**, *69*, 3261.
DOI: [10.1063/1.348546](https://doi.org/10.1063/1.348546)
28. Burke, L.D.; O'Sullivan, E.J.M. *J. Electroanal. Chem.* **1980**, *111*, 383.
DOI: [10.1016/S0022-0728\(80\)80059-3](https://doi.org/10.1016/S0022-0728(80)80059-3)
29. Andrukaitis, E.; Bishenden, E.A.; Jacobs, P.W.M.; Lorimer, J.W. *J. Power Sources* **1989**, *26*, 475.
DOI: [10.1016/0378-7753\(89\)80167-3](https://doi.org/10.1016/0378-7753(89)80167-3)
30. Livage, J.; Henry, M.; Sanchez, C. *Prog. Solid State Ch.* **1988**, *18*, 259.
DOI: [10.1016/0079-6786\(88\)90005-2](https://doi.org/10.1016/0079-6786(88)90005-2)
31. Shimizu, Y.; Nagase, K.; Miura, N.; Yamazoe, N. *Solid State Ionics* **1992**, *53-56*, 490.
DOI: [10.1016/0167-2738\(92\)90419-P](https://doi.org/10.1016/0167-2738(92)90419-P)
32. Wang, Z.; Chen, J.; Hu, X. *Thin Solid Films* **2000**, *375*, 238.
DOI: [10.1016/S0040-6090\(00\)01335-3](https://doi.org/10.1016/S0040-6090(00)01335-3)
33. Delmas, C.; Cognac-Auradou, H.; Cocciantelli, J.M.; Ménétrier, M.; Doumerc, J.P. *Solid State Ionics* **1994**, *69*, 257.
DOI: [10.1016/0167-2738\(94\)90414-6](https://doi.org/10.1016/0167-2738(94)90414-6)
34. Kwolek, P.; Oszejka, M.; Szacilowski, K. *Coordin. Chem. Rev.* **2012**, *256*, 1706.
DOI: [10.1016/j.ccr.2012.03.028](https://doi.org/10.1016/j.ccr.2012.03.028)
35. Galy, J. *J. Solid State Chem.* **1992**, *100*, 229.
DOI: [10.1016/0022-4596\(92\)90097-F](https://doi.org/10.1016/0022-4596(92)90097-F)
36. Cocciantelli, J.M.; Doumerc, J.P.; Pouchard, M.; Broussely, M.; Labat, J. *J. Power Sources* **1991**, *34*, 103.
DOI: [10.1016/0378-7753\(91\)85029-V](https://doi.org/10.1016/0378-7753(91)85029-V)
37. Cava, R.J.; Santoro, A.; Murphy, D.W.; Zahurak, S.M.; Fleming, R.M.; Marsh, P.; Roth, R.S. *J. Solid State Chem.* **1986**, *65*, 63.
DOI: [10.1016/0022-4596\(86\)90089-7](https://doi.org/10.1016/0022-4596(86)90089-7)
38. Labat, J.; Cocciantelli, J.M. French Patent 8916337, **1989**.
39. West, K.; Zachau-Christiansen, B.; Jacobsen, T.; Skaarup, S. *Electrochim. Acta* **1993**, *38*, 1215.
DOI: [10.1016/0013-4686\(93\)80052-2](https://doi.org/10.1016/0013-4686(93)80052-2)
40. Livage, J. *Coordin. Chem. Rev.* **1999**, *190-192*, 391.
DOI: [10.1016/S0010-8545\(99\)00096-X](https://doi.org/10.1016/S0010-8545(99)00096-X)
41. Livage, J.; Pelletier, O.; Davidson, P. *J. Sol.-Gel Sci. Technol.* **2000**, *19*, 275.
DOI: [10.1023/A:1008713127620](https://doi.org/10.1023/A:1008713127620)
42. Yao, T.; Oka, Y.; Yamamoto, N. *J. Mater. Chem.* **1992**, *2*, 337.
DOI: [10.1039/JM9920200337](https://doi.org/10.1039/JM9920200337)
43. Giorgetti, M.; Passerini, S.; Smyl, W.H. *Inorg. Chem.* **2000**, *39*, 1514.
DOI: [10.1021/ic9913233](https://doi.org/10.1021/ic9913233)
44. Takahashi, K.; Limmer, S.J.; Wang, Y.; Cao, G.Z. *Jpn. J. Appl. Phys.* **2005**, *44*, 662.
DOI: [10.1143/JJAP.44.662](https://doi.org/10.1143/JJAP.44.662)
45. Li, N.; Patrissi, C.J.; Martin, C.R. *J. Electrochem. Soc.* **2000**, *147*, 2044.
DOI: [10.1149/1.1393483](https://doi.org/10.1149/1.1393483)
46. Sides, C.R.; Martin, C.R. *Adv. Mater.* **2005**, *17*, 125.
DOI: [10.1002/adma.200400517](https://doi.org/10.1002/adma.200400517)
47. Ajayan, P.M.; Stephan, O.; Redlich, P.; Colliex, C. *Nature* **1995**, *375*, 564.
DOI: [10.1038/375564a0](https://doi.org/10.1038/375564a0)
48. Wang, Y.; Takahashi, K.; Shang, H.; Cao, G.Z. *J. Phys. Chem. B* **2005**, *109*, 3085.
DOI: [10.1021/jp044286w](https://doi.org/10.1021/jp044286w)
49. Patzke, G.R.; Krumeich, F.; Nesper, R. *Angew. Chem. Int. Ed.* **2002**, *41*, 2446.
DOI: [10.1002/1521-3773\(20020715\)41:14<2446::AID-ANIE2446>3.0.CO;2-K](https://doi.org/10.1002/1521-3773(20020715)41:14<2446::AID-ANIE2446>3.0.CO;2-K)
50. Pan, D.; Zhang, S.; Chen, Y.; Hou, J.G. *J. Mater. Res.* **2002**, *17*, 1981.
DOI: [10.1557/JMR.2002.0293](https://doi.org/10.1557/JMR.2002.0293)
51. Schlecht, U.; Knez, M.; Duppel, V.; Kienle, L.; Burghard, M. *Appl. Phys. A* **2004**, *78*, 527.
DOI: [10.1007/s00339-003-2383-2](https://doi.org/10.1007/s00339-003-2383-2)
52. Chang, Y.J.; Kang, B.H.; Kim, G.T.; Park, S.J.; Ha, J.S. *Appl. Phys. Lett.* **2004**, *84*, 5392.
DOI: [10.1063/1.1767284](https://doi.org/10.1063/1.1767284)
53. Gu, G.; Schmid, M.; Chiu, P.W.; Minett, A.I.; Fraysse, J.; Kim, G.T.; Roth, S.; Kozlov, M.; Munoz, E.; Baughman, R.H. *Nat. Mater.* **2003**, *2*, 297.
DOI: [10.1038/nmat880](https://doi.org/10.1038/nmat880)
54. Mai, L.; Xu, L.; Han, C.; Xu, X.; Luo, Y.; Zhao, S.; Zhao, Y. *Nano Lett.* **2010**, *4750-4755*, 10.
DOI: [10.1021/nl103343w](https://doi.org/10.1021/nl103343w)
55. Nesper, R.; Spahr, M.E.; Niederberger, M.; Bitterli, P.; *Nanotubes*, Int. Patent Appl. PCT/CH97/00470, **1997**.
56. Pillai, K.S.; Krumeich, F.; Muhr, H.-J.; Niederberger, M.; Nesper, R. *Solid State Ionics*, **2001**, *141-142*, 185.
DOI: [10.1016/S0167-2738\(01\)00757-3](https://doi.org/10.1016/S0167-2738(01)00757-3)
57. Sun, D.; Kwon, C.W.; Baure, G.; Richman, E.; MacLean, J.; Dunn, B.; Tolbert, S.H. *Adv. Funct. Mater.* **2004**, *14*, 1197.
DOI: [10.1002/adfm.200400056](https://doi.org/10.1002/adfm.200400056)
58. Li, G.; Pang, S.; Jiang, L.; Guo, Z.; Zhang, Z. *J. Phys. Chem. B* **2006**, *110*, 9383.
DOI: [10.1021/jp060904s](https://doi.org/10.1021/jp060904s)
59. Cao, A.M.; Hu, J.S.; Liang, H.P.; Wan, L.J. *Angew. Chem. Int. Ed.* **2005**, *44*, 4391.
DOI: [10.1002/anie.200500946](https://doi.org/10.1002/anie.200500946)
60. Li, B.; Xu, Y.; Rong, G.; Jing, M.; Xie, Y. *Nanotechnology*, **2006**, *17*, 2560.
DOI: [10.1088/0957-4484/17/10/020](https://doi.org/10.1088/0957-4484/17/10/020)
61. Chan, C.K.; Peng, H.; Tweten, R.D.; Jarausch, K.; Zhang, X.F.; Cui, Y. *Nano Lett.* **2007**, *7*, 490.
DOI: [10.1021/nl062883j](https://doi.org/10.1021/nl062883j)
62. Wang, Y.; Cao, G. *IEEE Nanotechnology Magazine*, **2009**, *14-20*.
DOI: [10.1109/MNANO.2009.932418](https://doi.org/10.1109/MNANO.2009.932418)
63. Takahashi, K.; Wang, Y.; Cao, G.Z. *J. Phys. Chem. B* **2005**, *109*, 48.
DOI: [10.1021/jp044772j](https://doi.org/10.1021/jp044772j)
64. Wang, Y.; Cao, G. *Adv. Mater.* **2008**, *20*, 2251.
DOI: [10.1002/adma.200702242](https://doi.org/10.1002/adma.200702242)
65. Dong, W.; Sakamoto, J.; Dunn, B. *J. Sol-Gel Sci. Techn.* **2003**, *26*, 641.
DOI: [10.1023/A:1020796626440](https://doi.org/10.1023/A:1020796626440)
66. Augustyn, V.; Dunn, B. *C. R. Chimie* **2010**, *13*, 130.
DOI: [10.1016/j.crci.2009.05.002](https://doi.org/10.1016/j.crci.2009.05.002)
67. Conway, B.E. *J. Electrochem. Soc.* **1991**, *138*, 1539.
DOI: [10.1149/1.2085829](https://doi.org/10.1149/1.2085829)
68. Rolison, D.R.; Dunn, B. *J. Mater. Chem.* **2001**, *11*, 963.
DOI: [10.1039/B007591O](https://doi.org/10.1039/B007591O)
69. Harreld, J.H.; Dong, W.; Dunn, B. *Mater. Res. Bull.* **1998**, *33*, 561.
DOI: [10.1016/S0025-5408\(98\)00022-1](https://doi.org/10.1016/S0025-5408(98)00022-1)
70. Takahashi, K.; Wang, Y.; Cao, G.Z. *Appl. Phys. Lett.* **2005**, *86*, 053 102.
DOI: [10.1063/1.1857087](https://doi.org/10.1063/1.1857087)
71. Cheng, K.-C.; Chen, F.-R.; Kai, J.-J. *Sol. Energ. Mat. Sol. C.* **2006**, *90*, 1156.
DOI: [10.1016/j.solmat.2005.07.006](https://doi.org/10.1016/j.solmat.2005.07.006)

